

Observational tests of the black hole area increase law

Miriam Cabero,^{1,2, a} Collin D. Capano,^{1,2} Ofek Fischer-Birnholtz,^{1,2} Badri Krishnan,^{1,2} Alex B. Nielsen,^{1,2} Alexander H. Nitz,^{1,2} and Christopher M. Biwer^{3,4}

¹Max Planck Institute for Gravitational Physics (Albert Einstein Institute), Callinstrasse 38, D-30167 Hannover, Germany

²Leibniz Universität Hannover, Welfengarten 1-A, D-30167 Hannover, Germany

³Department of Physics, Syracuse University, Syracuse, NY 13244, USA

⁴Applied Computer Science (CCS-7), Los Alamos National Laboratory, Los Alamos, NM 87545, USA

(Dated: July 31, 2018)

The black hole area theorem implies that when two black holes merge, the area of the final black hole should be greater than the sum of the areas of the two original black holes. We examine how this prediction can be tested with gravitational-wave observations of binary black holes. By separately fitting the early inspiral and final ringdown stages, we calculate the posterior distributions for the masses and spins of the two initial and the final black holes. This yields posterior distributions for the change in the area and thus a statistical test of the validity of the area increase law. We illustrate this method with a GW150914-like binary black hole waveform calculated using numerical relativity, and detector sensitivities representative of both the first observing run and the design configuration of Advanced LIGO. We obtain a $\sim 74.6\%$ probability that the simulated signal is consistent with the area theorem with current sensitivity, improving to $\sim 99.9\%$ when Advanced LIGO reaches design sensitivity. An important ingredient in our test is a method of estimating when the post-merger signal is well-fit by a damped sinusoid ringdown waveform.

I. INTRODUCTION

The black hole area increase law [1, 2] is one of the most celebrated results in exact non-linear relativity. It applies to both single black holes and to mergers of multiple black holes and implies that the total horizon areas should always increase provided certain assumptions that are expected to hold for astrophysical black holes. This law suggests an analogy between the area of the horizon of a black hole and its entropy [3–5], and is thus one of the central results of black hole thermodynamics. The observations of gravitational waves from binary black hole coalescence events [6–10] open up the possibility of carrying out direct tests of this fundamental law using observational data. In this paper we shall present a method to perform such a test based on the inspiral and on the ringdown stages of simulated binary black hole coalescences.

Gravitational-wave observations of binary black hole coalescences correspond to the inspiral of two black holes that merge together to form a single black hole which then settles down to a stationary state by a ringdown process. The areas of the black hole horizons are not directly observable using gravitational wave data, so here we make use of the Kerr metric to relate the black hole horizon area to its asymptotic mass M and dimensionless spin χ . Widely separated inspiralling black holes are expected to be very well described by the Kerr metric in some neighbourhood of the horizon. Mass and spin values can be inferred for the inspiralling black holes by comparison with inspiral gravitational waveforms. The mass and spin of the final black hole can be inferred by

comparison with ringdown waveforms of a single Kerr black hole.

If two initially distant Kerr black holes with areas A_1, A_2 coalesce to form a final Kerr black hole with area A_f , then it follows from the area increase law that

$$A_1 + A_2 \equiv A_i < A_f. \quad (1)$$

Our analysis strategy is similar to the suggestion by Hughes and Menou [11], namely, use the early inspiral regime to measure the parameters of the initial black holes, and independently use the late-time ringdown regime to measure the parameters of the final black hole. The end result of the parameter estimation procedure will be a probability distribution $p(\Delta A)$ for the change in the area $\Delta A := A_f - (A_1 + A_2)$. This allows us to calculate a probability

$$\int_0^\infty p(\Delta A) d\Delta A \quad (2)$$

that a particular event is compatible with the area increase law.

By analysing the observed gravitational wave data for the detected events [6–10, 12], posterior distributions for the parameters of the initial and final black holes in these events have been reported in [8–10, 13]. However, these cannot be used as an independent test of the area increase law because these results use fitting formulae to obtain the final M_f, χ_f (and thus A_f) as functions of the initial parameters. These fitting formulae [14–16] are results of numerical relativity simulations which assume the validity of vacuum general relativity, and thus implicitly assume *a priori* the validity of the area increase law. A true direct test of the area increase law should independently obtain A_i and A_f from the observed data and then use them to verify whether or not Eq.(1) holds.

^a miriam.cabero@aei.mpg.de

Similarly, tests have been designed to check the consistency between the inspiral and merger-ringdown parts of gravitational wave signals [17, 18]. When performed on gravitational wave observations these tests have found the signals to be compatible with standard general relativity and the fitting formulae [6, 8–10]. Our proposed test here is different in that we avoid the use of fitting formulae entirely; we separate the signal in the time domain rather than the frequency domain, and crucially we avoid using data from the near merger portion of the signal. A violation of the area theorem is perhaps most likely near the merger of the two black holes where the spacetime is most dynamic. It is this region where numerical relativity simulations are critical to follow the evolution. We wish to avoid this region and infer areas for the inspiralling black holes only from the early inspiral phase when the two black holes are clearly separated and infer the area of the final black hole only from its simple ringdown behaviour as given by the Kerr metric.

Another result that shows up naturally is an independent estimate of the energy radiated away during the merger in the form of gravitational radiation without using any of the aforementioned numerical relativity fits. Since we obtain the two initial masses and the final mass, it is straightforward to compute the difference and obtain a posterior distribution of the radiated energy. This can be compared with the numerical relativity prediction and thus offers yet another test of general relativity.

The various details involved in this calculation will be described in the following sections. The plan for the rest of the paper is as follows. Sec. II introduces preliminary material and notation. Sec. III presents the details of the test. Sec. IV and Sec. V present results on simulated signals and finally Sec. VI has concluding remarks on the future prospects of this test.

II. PRELIMINARIES

A. Testing the assumptions

A test of the black hole area increase theorem is a test of whether the assumptions that go into the theorem’s proof are valid. Any violation of area increase would be proof that at least one of the assumptions does not hold. In the test proposed here, we measure the change in area between two asymptotic states, well before the merger and well after the merger, where the relevant black holes can be approximated by Kerr black holes. It is therefore not a test that the total horizon area is increasing at all times during the coalescence. However, the change in area between these asymptotic states can be written as a time integral over the instantaneous rate of area change and hence our test depends on the assumptions used to show that the rate of area change should always be positive. A decrease in the area between asymptotic states would be a demonstration that at least one of these assumptions was violated (although clearly if the overall

area change is positive this does not necessarily preclude that the area was decreasing at some point during the merger, or indeed that some of the assumptions were mildly violated but the area still increases).

There exist in the literature several different proofs of the area increase law that can be classified according to which type of horizon they refer to, the main classes being event horizons and quasi-local horizons based on the notion of marginally trapped surfaces/apparent horizons. The proofs of the area increase law make different assumptions in either of the two cases. In the asymptotic states considered here, both when the two black holes are far apart and at late times when the final black hole is in equilibrium, there is no difference between the areas of the event horizon or quasi-local horizons. Thus if the overall area change is measured to be negative then this would be a violation both of proofs using event horizons and of those using quasi-local horizons, and therefore at least one of the common assumptions would most likely be violated (although it is logically possible that different assumptions are violated in the two cases).

Proofs of the area increase law for event horizons (see e.g. [19]) rely on three main ingredients:

i) The null curvature condition, which says that the Ricci tensor $R_{\mu\nu}$ must satisfy $R_{\mu\nu}\xi^\mu\xi^\nu \geq 0$ for any null vector field ξ^μ . While the area theorem does not depend on the Einstein equations, in Einstein’s general relativity this assumption is equivalent to the requirement that the stress-energy tensor T_{ab} satisfies the null energy condition $T_{\mu\nu}\xi^\mu\xi^\nu \geq 0$.

ii) Asymptotic flatness and additional global conditions which ensure that the spacetime outside the black hole (including the event horizon) must be predictable from suitable data on a Cauchy surface. In particular, these conditions rule out the presence of naked singularities (cosmic censorship).

iii) The proofs use properties of the intrinsic geometry of event horizons and in particular the geodesic deviation equation for null geodesics on the event horizon.

It can be shown that given the previous conditions, the congruence of null geodesics generating the event horizon cannot have negative expansion anywhere and the area is always increasing. The most general statement and proof of the area increase law is by Chrusciel et al [20]. This includes the cases when the event horizon is not smooth¹ and also applies to non-zero values of the cosmological constant. As expected, cosmic censorship and the null curvature condition are still required.

Since gravitational wave observations only probe a finite region of spacetime, it would seem unreasonable that we could say anything definite about naked singularities *anywhere* in the universe based on these observations.

¹ Generically event horizons are not smooth; cusps are formed when null geodesics enter the horizon [21]. Numerical relativists assume that the horizon is regular except for a finite number of such cusps (see e.g. [22]).

This is also an artefact of the well known global and teleological features of the event horizon. Thus, should we have observational evidence that the area increase law is violated, we can expect the energy condition to be the main culprit.

This can be seen clearly in alternate formulations of the area increase law. It is possible to formulate the area increase law for black holes in a quasi-local framework, without these global assumptions, relying on marginally trapped surfaces and the associated notions of dynamical and trapping horizons [23–25]. Using the Einstein equations on the horizon, it is possible to obtain a “physical process” version of the area increase law which relates the increase in area to the fluxes of in-falling matter and radiation [26]. These fluxes are manifestly positive if the dominant energy condition holds.

It is in fact known that energy conditions can be violated in nature by a number of mechanisms [27]. The question of whether sufficient energy condition violation occurs during a binary black hole merge to cause the horizon area to decrease is one of the main motivations for our test.

In our test of the area increase law, we shall assume that the black hole no-hair theorem holds, i.e. that any astrophysical *stationary* black hole is completely described by its mass M and angular momentum J and given by the Kerr solution. This applies to the two initial black holes and to the final black hole formed as a result of the coalescence. Thus, any cross-section of the black holes at early and late times has an area A given by

$$A = 8\pi M^2 \left(1 + \sqrt{1 - \chi^2}\right). \quad (3)$$

Here $\chi = J/M^2$ is the dimensionless spin, which can take values $-1 \leq \chi \leq 1$. It is an important goal to test whether the no-hair theorems are valid and in fact, there is a large body of work on possible tests of the black hole uniqueness theorem from binary black hole observations [28–33]. It would be preferable to drop this assumption and design a joint test of both the area increase law and the uniqueness theorems, but this is beyond the scope of the present paper. It is important for us to clearly identify the parts of the waveform when we cannot assume the no-hair theorem to hold and this will be addressed below in Secs. III B and III C.

As shown by Hawking [1], the constraint derived from the area increase law can be used to bound the amount of energy emitted during the coalescence process. For a coalescence of non-spinning, equal-mass black holes, this bound limits the emitted energy to be no more than about 29% of the initial rest-mass energy of the two black holes (see also [34]). Numerical simulations of black hole collisions show that in reality the amount of energy radiated by gravitational waves is considerably less than this theoretical upper bound [35].

B. Estimating the parameters

To extract the mass and spin parameters from the observations we must examine the nature of the gravitational waves produced. Consider a plane gravitational wave corresponding to a gravitational metric perturbation $h_{\mu\nu}$. We can find a frame transverse to the direction of propagation so that the transverse-traceless part of $h_{\mu\nu}$ can be written in terms of two polarisations:

$$h_+(t) = A_+(t) \cos \Phi(t), \quad (4)$$

$$h_\times(t) = A_\times(t) \sin \Phi(t). \quad (5)$$

Here $A_{+,\times}$ are slowly varying amplitudes and $\Phi(t)$ is a rapidly varying phase. The amplitudes depend on the intrinsic parameters of the source, the distance to the binary, and the angle between the line-of-sight vector from the binary to Earth and the orbital angular momentum vector (inclination angle ι).

The response of an interferometric detector to this wave depends on the relative orientation between the wave frame and the detector frame and thus is specified by three angles. These three angles are typically taken to be the sky-location of the source given by a right ascension α and declination δ in a geocentric coordinate system, and the so-called polarisation angle ψ defining the relative orientation of the wave frame with the geocentric coordinate system (see e.g. [36, 37]). Assuming the wavelength of the signal to be much larger than the detector arms, appropriate for ground based detectors and for the kind of signals we are considering, the strain $h(t)$ observed by the detector is

$$h(t) = F_+(\alpha, \delta, \psi)h_+(t-t_0, \phi_0) + F_\times(\alpha, \delta, \psi)h_\times(t-t_0, \phi_0). \quad (6)$$

Here $F_{+,\times}$ are the beam pattern functions of the detectors (assumed to be constant over the duration of the signal), t_0 is a suitably defined arrival time and ϕ_0 is the phase at t_0 . It is useful to rewrite $h(t)$ as

$$h(t) = A(t) \cos(\phi_0 + \phi(t-t_0)), \quad (7)$$

where $A(t)$ is a slowly varying amplitude and $\phi(t-t_0)$ a rapidly varying phase.

We estimate the source parameters of a gravitational wave signal using Bayesian inference, which was the method used to estimate the parameters of GW150914 and all subsequent events [13]. We wish to know the properties of the source of a gravitational-wave signal that exists in some given data $s(t)$. To that end, we use a model of the signal h that is parametrised by the source properties $\{M_1, \chi_1, \dots\} \equiv \vec{\vartheta}$. We cannot measure these properties to infinite precision. Instead we seek the probability density function $p(\vec{\vartheta}|s, h)$, which quantifies our measurement uncertainty. According to Bayes’ Theorem, $p(\vec{\vartheta}|s, h)$ (known as the *posterior* distribution) is proportional to the likelihood $\mathcal{L}(s|\vec{\vartheta}, h)$ of observing the data given $\vec{\vartheta}$ times a *prior* probability distribution $p(\vec{\vartheta})$.

The prior represents our knowledge of $\vec{\vartheta}$ before observing the data. In a network of N_d gravitational-wave detectors containing uncorrelated stationary Gaussian noise, the likelihood function is:

$$\mathcal{L}(s|\vec{\vartheta}, h) \propto \exp \left[-\frac{1}{2} \sum_{a=1}^{N_d} \langle h_a(\vec{\vartheta}) - s_a, h_a(\vec{\vartheta}) - s_a \rangle \right], \quad (8)$$

where s_a is the data in each detector and h_a is the model waveform (or *template*) as it would be observed in each detector. The inner product $\langle \cdot, \cdot \rangle$ is:

$$\langle x, y \rangle \equiv 4\Re \int_0^\infty \frac{\tilde{x}_a^*(f) \tilde{y}_a(f)}{S_n^{(a)}(f)} df. \quad (9)$$

Here $S_n^{(a)}(f)$ is the single-sided power spectral density (PSD) of the noise in the a -th detector.

Stochastic samplers based on Markov-chain Monte Carlo (MCMC) techniques can be used to evaluate Eq. (8) over the large, multidimensional space of possible parameters and produce an estimate of $p(\vec{\vartheta}|s, h)$. This estimate can then be numerically marginalised to yield Bayesian credible intervals on various parameters.

III. METHOD

Normally, when analysing the entire signal (and assuming the detector noise truly is stationary and Gaussian), the parameter estimates produced by the method described in Sec. IIB will be unbiased. In other words, if the source distribution is the same as the prior, then we can expect that a signal's true parameters will lie within the $X\%$ credible interval $X\%$ of the time.

However, the method described in Sec. IIB will yield biased estimates if a parameter-dependent cut is applied to the template waveforms [38], as we wish to do here. This is due to the fact that Eq. (8) is derived assuming that the template is a model for the entire signal; i.e., $\mathcal{L}(s|\vec{\vartheta}, h)$ is maximised for parameters that best match the signal averaged over the entire bandwidth of the detector. Here, however, we wish to find the parameters that best-match the signal only over a limited portion of the signal, while ignoring the rest. Crucially, the onset and duration of the part that we wish to exclude — the merger — is dependent on the signal's source parameters. Since this additional, parameter-dependent condition is not included in $p(\vec{\vartheta}|s, h)$, a naïve application of Eq. (8) results in biased measurements, as we will see below.

Further complicating our efforts is our desire to excise a part of the signal in the time domain rather than the frequency domain. As discussed below, this effectively couples the sky location of the signal to the measurement of the initial and final masses and spins.

In the following we describe a method to overcome these challenges. To illustrate and test the method, we simulate a signal using a publicly available waveform produced by the SXS collaboration [39, 40]. We choose a

non-spinning, equal-mass binary black hole² with total mass $M_t = 70M_\odot$.³ The signal, which is similar to a signal like GW150914, is injected in zero noise at a luminosity distance $D_L = 500$ Mpc.

We compare results using two different detector sensitivities: the PSD published in the LIGO Open Science Centre [42] for GW150914, which is representative of Advanced LIGO's first observing run, and the zero-detuned high-power (ZDHP) PSD [43], which is representative of LIGO's expected sensitivity in the coming years. In this analysis we only consider the two LIGO detectors. However, the method can be trivially expanded to include any number of detectors.

We use the PyCBC Inference framework to estimate $p(\vec{\vartheta}|s, h)$ [44]. This is a python-based pipeline similar to the LALInference pipeline [45] used to infer the parameters of published gravitational waves. PyCBC Inference supports multiple stochastic sampling engines. In this study we use `kombine` [46], which is an MCMC sampler that uses an ensemble of Markov chains (or *walkers*) to efficiently estimate $p(\vec{\vartheta}|s, h)$.

A. The effect of sky location

An integral part of our analysis is separating the inspiral part to estimate the initial parameters of the binary and the ringdown part to estimate the parameters of the final black hole. The templates used for the parameter estimation are terminated (or started) at a specific time. This method complicates the issue of dealing with the sky location since the sky location affects the arrival time of the signal in the detectors.

We have found that if the sky location is allowed to vary in the MCMC, the terminated templates will favour sky locations that get them closer to the merger, yielding biased results. One could fix the sky location to a single point if it were known. However, we do not expect to measure the sky location of a binary black hole merger to sufficient precision with the current network of gravitational-wave detectors for this approach to work. Indeed, when doing the ringdown analysis, we have found that choosing different fixed points drawn from within the 50% credible interval of the sky location produced by a full inspiral-merger-ringdown analysis yields statistically significant different estimates of the final mass and spin. Thus picking a single point for the sky location when one is not actually known will result in an underestimate of our uncertainty, and a potential bias, of these parameters.

² Numerical waveform SXS:BBH:0066, Lev5

³ Since we use waveform templates that do not include subdominant modes, we select only the 22 mode of the numerical waveform. This is a sensible approach because higher modes are not expected to be detectable with current sensitivities [28, 41].

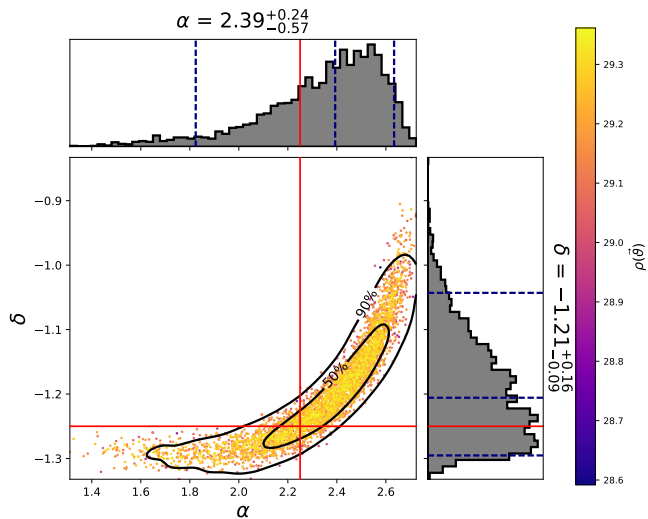


FIG. 1. Posterior distribution for the sky location (right ascension α and declination δ) obtained from the full simulated signal. The colorbar shows the signal-to-noise ratio (SNR), which is a function of the likelihood, and the red lines indicate the values that were injected. The centre and outer dashed lines in the histograms represent the median value and the 90% credible interval, respectively. These correspond to the values and the errors given on top of the histograms.

To account for this uncertainty, we fix the sky location to a distribution rather than a single point when doing the inspiral and ringdown analyses. We do this by assigning each walker in our MCMC to a different right ascension and declination. These locations are drawn from a given sky map that quantifies the uncertainty in the event’s location. The walker’s positions in the sky remain fixed throughout the entirety of the parameter estimation routine. This way, we include all the information obtained from allowing the sky location to vary without forcing the entire parameter estimation analysis to remain on one fixed point.

We use the same sky locations for the inspiral and ringdown analysis. After evolving the MCMC until it is burned in, each walker in the inspiral (ringdown) analysis produces a point estimate of the initial (final) area. Taking the estimates over all of the walkers produces a distribution of areas. When taking the difference in areas, we only compare point estimates between the same sky locations in both runs. Thus, the inspiral and ringdown analyses are independent in all parameters except for the sky location.

To produce a sky map for this study, we first perform the parameter estimation analysis on the full signal, using full inspiral-merger-ringdown IMRPhenomD templates [47, 48]. Figure 1 shows the marginalised posterior distribution of the right ascension (α) and declination (δ) obtained from this analysis. We only use the sky-location information from this analysis; no information regarding the GW parameters $\vec{\vartheta}$ are kept. Here, we have restricted

our analysis to the two LIGO detectors. However it is trivial to include a third detector, if available, to improve our measurement of the sky location [10, 12].

Since the sky location relies primarily on the time of arrival of the signal at different detectors, it is possible to estimate the sky location using searches that do not use any waveform models from general relativity. For example, a sky map produced using the coherent Wave Burst pipeline [49] was published with GW150914 [42]. The sky map produced by this pipeline may be used when applying our test to real events.

B. The inspiral analysis

The initial parameters ought to be measured from the inspiral part of the waveform, with no assumptions or input from the merger or ringdown. Ideally, one would use post-Newtonian waveforms [50]. However, full inspiral-merger-ringdown waveforms such as the IMRPhenomD family [47, 48] have better agreement with numerical relativity waveforms at higher inspiral frequencies. We shall use IMRPhenomD waveforms terminated at the end of the inspiral to exclude the highly dynamical merger phase and guarantee that the inspiral analysis is completely independent from the merger and ringdown. For compact binaries with arbitrary masses and spins, the hybrid minimum energy circular orbit (hybrid MECO) [51] is a proxy for the end of the inspiral. The hybrid MECO depends on the mass ratio of the binary and on the spins of the black holes, and is symmetric under exchange of the individual objects’ parameters.

Näively, one might think that to exclude the merger phase from the analysis, we need only to terminate the templates at the time at which they pass through hybrid MECO. However, while this excludes the merger dynamics in the templates, it does not exclude the merger in the signal. This results in templates with higher spin and mass matching the signal better than the template that has the same mass and spin of the signal, leading to biased results. This is because the hybrid MECO of these templates occurs at a higher frequency. Effectively, these templates are able to see more of the signal; the additional signal-to-noise ratio (SNR) they gain in doing so is enough to offset any mismatch these templates have with the signal at lower frequencies.

To recover the correct masses and spins it is necessary to exclude the merger dynamics in both the templates and the signal. However, because the intrinsic parameters of the signal are unknown, the time at which the signal passes through hybrid MECO is also unknown. To estimate this time we choose a grid of times $t_{\text{grid}} < t_{\text{ref}}$, where t_{ref} is a fiducial time chosen arbitrarily in the proximity of the expected coalescence time of the binary. We perform an independent parameter estimation analysis for each grid time. In each analysis, we apply a taper function to the templates in the time domain that goes to zero at a time t_{taper} . The taper time is varied across

parameter space and between detectors. Specifically, for a given set of parameters $\vec{\vartheta}$ and a detector D,

$$t_{\text{taper}} = \min \left[t_{\text{grid}} + \delta t(\alpha, \delta; D), t_{\text{hMECO}}(\vec{\vartheta}) \right], \quad (10)$$

where t_{hMECO} is the time at which the template goes through hybrid MECO. The $\delta t(\alpha, \delta; D)$ is an offset applied to account for the arrival time uncertainty in each detector arising from the uncertainty in sky location.

When doing the analysis we found that whitening the template before tapering yielded better results than simply applying the taper to the waveform and then whitening. That is, we replace the full IMR template h with:

$$h'(t) = w(t; t_{\text{taper}})[h * \widetilde{A^{-1}}](t),$$

where $\widetilde{A^{-1}}(t)$ is the inverse Fourier transform of $1/\sqrt{S_n(f)}$; the $*$ indicates convolution. We use half a Kaiser window with a duration of 10 ms and shape parameter $\beta = 8$ [52] for the taper function $w(t; t_{\text{taper}})$. A duration of 10 ms is used because the whitening filter $\widetilde{A^{-1}}(t)$ effectively goes to zero on this time scale, ensuring that times $t > t_{\text{taper}}$ are minimally coupled to times $t < t_{\text{taper}}$ via the convolution. The whitened, tapered template $h'(t)$ is filtered with the whitened data.

The grid time t_{grid} prevents the templates from matching the merger dynamics in the signal. For t_{grid} times later than t_{hMECO} , results are influenced by the dynamic merger phase and the posterior distributions yield biased results. As t_{grid} approaches t_{hMECO} of the signal, the posterior settles around the parameters of the signal. For t_{grid} times earlier than the signal's t_{hMECO} , the posterior remains in the same region of parameter space, though it begins to widen due to the decreasing SNR. Therefore, the transition time between the moving and the growing posterior distributions yields the best point at which to calculate the initial areas.

It is thus clear that to estimate the transition time, we need to study how the posterior distributions change as t_{grid} is varied. A general notion of the divergence between two probability distributions $p_1(x)$ and $p_2(x)$ is provided by the Kullback-Leibler divergence (see e.g. [53]) which, for discrete distributions is defined as

$$D_{KL}(p_1||p_2) = \sum_x p_1(x) \log \frac{p_1(x)}{p_2(x)}. \quad (11)$$

However $D_{KL}(p_1||p_2)$ is not symmetric, i.e. $D_{KL}(p_1||p_2) \neq D_{KL}(p_2||p_1)$. In particular, D_{KL} cannot be viewed as a distance between probability distributions. D_{KL} is an appropriate divergence to use when one of the distributions is privileged for some reason.

In our case, we have no reason to distinguish different values of $t_{\text{ref}} - t_{\text{grid}}$ and thus we choose to use instead the Jensen-Shannon (JS) divergence. Given two probability distributions p_1 and p_2 , the JS divergence is a symmetric

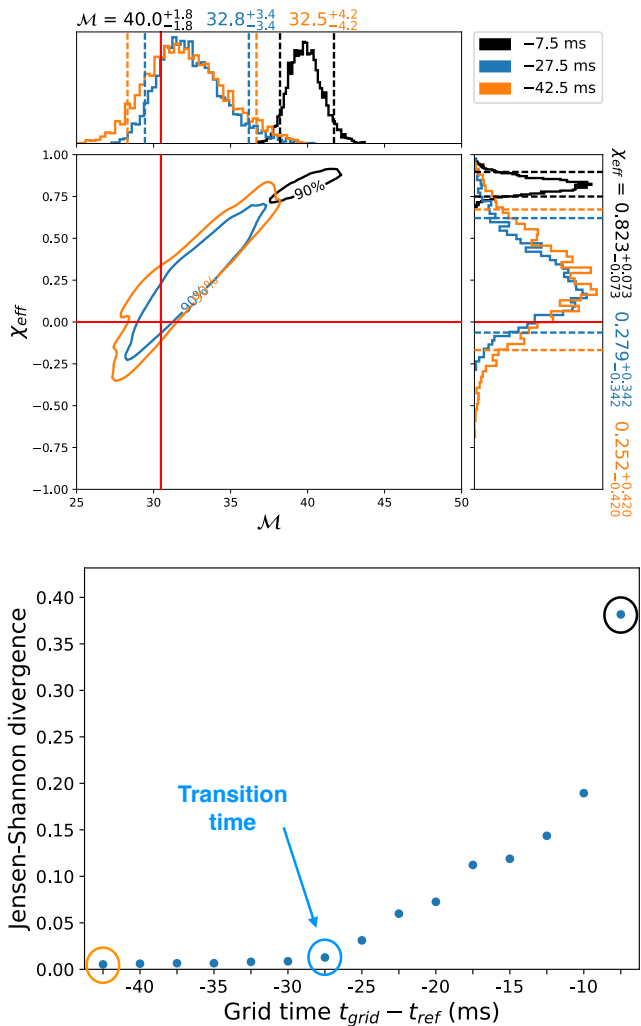


FIG. 2. (Top) Posterior distribution of the chirp mass and the effective spin obtained from three different runs. The red cross indicates the injected values. (Bottom) Jensen-Shannon divergence between consecutive grid runs. The x -axis indicates the corresponding time t_{grid} and the JS divergence is calculated between the posterior distributions at t_{grid} and $t_{\text{grid}} + \Delta t$, where $\Delta t = 2.5$ ms. The coloured circles indicate the times corresponding to the posterior distributions in the top figure. The chosen transition time is $t_{\text{grid}} - t_{\text{ref}} = -27.5$ ms.

and smooth version of the Kullback-Leibler (KL) divergence $D_{KL}(p_1||p_2)$:

$$D_{JS}(p_1||p_2) = \frac{1}{2}D_{KL}(p_1||q) + \frac{1}{2}D_{KL}(p_2||q), \quad (12)$$

where $q = \frac{1}{2}(p_1 + p_2)$. It has been shown that D_{JS} can be turned into a distance measure between probability distributions [54].

Figure 2 shows the JS divergence between the posterior distribution of the analysis at t_{grid} and the analysis at $t_{\text{grid}} + \Delta t$, which we have chosen to be $\Delta t = 2.5$ ms. Since we are only interested in the masses and

spins of the black holes, we compute the JS divergence using the 2D marginalised distribution of chirp mass $\mathcal{M} = (M_1 M_2)^{3/5} / M_t^{1/5}$ and effective spin $\chi_{\text{eff}} = (M_1 \chi_1 + M_2 \chi_2) / M_t$. While the posterior distribution is still moving, the JS divergence is changing significantly. The transition time is given by the maximum inspiral (minimum ringdown) grid time where the JS divergence is still roughly constant. From Figure 2, the transition time is clearly seen to be at the time $t_{\text{grid}} = t_{\text{ref}} - 27.5$ ms. At times closer to the merger, the difference between consecutive JS divergences increases significantly.

In doing the analysis shown in Fig. 2, we vary the two component masses $M_{1,2}$, two component spins $\chi_{1,2}$, distance D_L , inclination ι , polarisation ψ , coalescence phase ϕ_0 , and the template's coalescence time t_c . We use uniform priors for all of these parameters. The prior range for the parameters of interest is $M_i \in [10, 80] M_\odot$ and $\chi_i \in [-0.9895, 0.9895]$. This is the same prior that was used in the analysis of GW150914 [13].

C. The ringdown analysis

The late ringdown phase is well described through perturbation theory. Assuming that the final object is a Kerr black hole, the ringdown signal consists of a sum of exponentially damped sinusoids [55]. It is natural to write the gravitational wave in terms of spin-weighted spheroidal harmonics:

$$h_+ + ih_\times = \sum_{\ell, m, n} {}_{-2}S_{\ell m}(\iota, \varphi) A_{\ell m n} e^{i(\Omega_{\ell m n} t + \phi_{\ell m n})}. \quad (13)$$

The sum in the above equation is over the quantum numbers ℓ, m and the overtone n . Thus, $m = -\ell, -\ell + 1, \dots, 0, \dots, \ell$ for each $\ell = 2, 3, \dots$ and $n = 0, 1, 2, \dots$. The angular functions ${}_{-2}S_{\ell m}(\iota, \varphi)$ are the spin-weighted spheroidal harmonics which appear as the angular eigenfunctions of the equations describing the gravitational perturbations of a Kerr black hole found by Teukolsky (see e.g. [56]). These functions depend on the angular momentum and mass of the Kerr black hole and reduce to the usual spin-weighted spherical harmonics for the non-spinning case. The inclination angle ι is the angle between the line-of-sight vector from the black hole to Earth and the intrinsic angular momentum of the black hole, and φ is the azimuth angle of the black hole with respect to the observer. The amplitudes $A_{\ell m n}$ and the phases $\phi_{\ell m n}$ are arbitrary as far as our ringdown analysis is concerned. In principle they depend on the configuration of the gravitational perturbation $h_{\mu\nu}$ at the beginning of the ringdown phase (when linear perturbation theory begins to be applicable) which in turn depends on the initial configuration of the binary and on the particular gravitational theory. However, we shall make no assumption relating the amplitudes or phases to the initial parameters of the binary. The complex frequencies $\Omega_{\ell m n}$ are the quasi-normal frequencies determined from the Teukolsky equation. They are the frequencies for

which we obtain solutions which are purely outgoing at infinity and purely ingoing at the horizon. See [57] for a method of calculating these frequencies for a Kerr black hole and see e.g. [30, 58] for reviews on black hole ringdown.

The two polarisations of the gravitational waveform are given by

$$\begin{aligned} h_+(t) &= \sum_{\ell, m, n} {}_{-2}Y_{\ell m}^+(t) A_{\ell m n} e^{-t/\tau_{\ell m n}} \cos(\omega_{\ell m n} t + \beta_{\ell m n}), \\ h_\times(t) &= \sum_{\ell, m, n} {}_{-2}Y_{\ell m}^\times(t) A_{\ell m n} e^{-t/\tau_{\ell m n}} \sin(\omega_{\ell m n} t + \beta_{\ell m n}). \end{aligned} \quad (14)$$

It is assumed here that the ringdown begins at $t = 0$ and instead of the complex frequency $\Omega_{\ell m n}$ we have used the damping time $\tau_{\ell m n}$ and real frequency $\omega_{\ell m n}$. Here, we have approximated spin-weighted spheroidal harmonics ${}_{-2}S_{\ell m n}$ by spin-weighted spherical harmonics ${}_{-2}Y_{\ell m n}$ [59, 60]. The angle $\beta_{\ell m n} = \phi_{\ell m n} + m\varphi$ combines the initial ringdown phase with the azimuthal part of the spherical harmonics, and we have defined [60]

$$\begin{aligned} {}_{-2}Y_{\ell m}^+(t) &= {}_{-2}Y_{\ell m}(t, 0) + (-1)^\ell {}_{-2}Y_{\ell -m}(t, 0), \\ {}_{-2}Y_{\ell m}^\times(t) &= {}_{-2}Y_{\ell m}(t, 0) - (-1)^\ell {}_{-2}Y_{\ell -m}(t, 0). \end{aligned} \quad (15)$$

Throughout this paper we use only the fundamental mode ($\ell = m = 2, n = 0$). However, the methods presented here can be extended to multi-mode ringdowns once the detectors' sensitivities allow the detectability of higher order modes.

The ringdown template assumes $h(t) = 0$ before the start of the damped sinusoid, but it is unknown in the data when the signal waveform starts behaving like a pure damped sinusoid. Same as for the inspiral phase, we choose a grid of times $t_{\text{grid}} > t_{\text{ref}}$ and perform the ringdown analysis for each time separately, where t_{ref} is the same fiducial time used for the inspiral analysis. Times closer to the coalescence of the signal will again show biased results. If t_{ref} is after the coalescence time of the signal, we might have to use a few times $t_{\text{grid}} < t_{\text{ref}}$ to find the transition time. Figure 3 shows the resulting JS divergence between the posterior distribution of the analysis at t_{grid} and the analysis at $t_{\text{grid}} + \Delta t$, which for the ringdown analysis we have chosen to be $\Delta t = 0.5$ ms. The JS divergence is computed using the 2D marginalised distribution of final mass M_f and final spin χ_f . The transition time in the ringdown analysis happens at the time $t_{\text{grid}} = t_{\text{ref}} + 0.5$ ms.

We find that it is necessary to zero out the data prior to the grid time in order to accurately recover the final mass and spin using the damped sinusoid. This is different than the inspiral analysis, in which only the templates were modified. As discussed above, the time domain representation of the whitening filter $\hat{A}^{-1}(t)$ has non-zero support on time scales $\mathcal{O}(\text{ms})$. This is significant in the ringdown analysis, in which differences of a few milliseconds can have large effects on the estimated parameters.

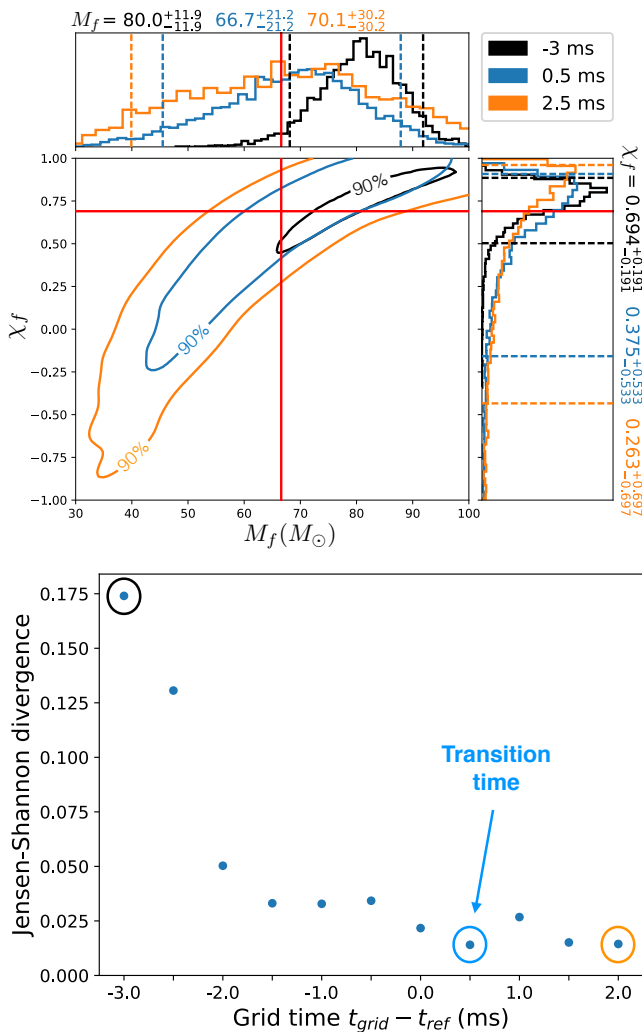


FIG. 3. (Top) Posterior distribution of the final mass M_f and the final spin χ_f obtained from three different runs. The red cross indicates the injected values. (Bottom) Jensen-Shannon divergence between consecutive grid runs. The x -axis indicates the corresponding time t_{grid} and the JS divergence is calculated between the posterior distributions at t_{grid} and $t_{\text{grid}} + \Delta t$, where $\Delta t = 0.5$ ms. The coloured circles indicate the times corresponding to the posterior distributions in the top figure. The chosen transition time is $t_{\text{grid}} - t_{\text{ref}} = 0.5$ ms.

Namely, the convolution of the whitening filter with the signal in Eq. (9) couples information from the merger with the post-merger ringdown. Since the damped sinusoid is simply zero prior to its onset, the whitening filter has a different effect on it. Thus, even if the template and the post-merger signal are exactly the same prior to whitening, they are different afterward. This difference particularly biases the recovered damping time, which in turn affects the estimated final mass and spin. Zeroing out the data prior to whitening decouples the whitened signal’s merger and ringdown, and causes the whitening filter to affect the signal and template in the same way,

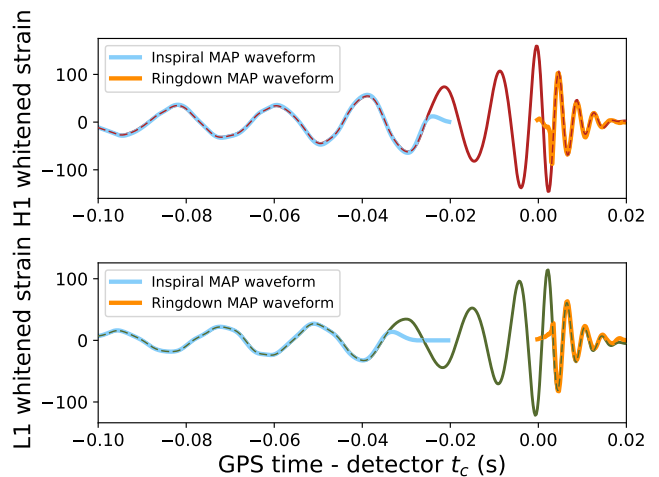


FIG. 4. Whitened strain in each detector with the maximum posterior (MAP) waveform from the inspiral analysis (blue) and from the ringdown analysis (orange).

correcting the bias.

The variable parameters for the ringdown analysis are the central frequency $f_{220} = \omega_{220}/2\pi$, damping time τ_{220} , amplitude A_{220} , phase β_{220} , inclination ι and polarisation ψ (we drop the 220 label from now onwards). We use uniform priors for all of these parameters. Using the fitting formulae in [61], one can obtain the final black-hole’s mass M_f and spin χ_f from the ringdown frequency and damping time. The prior range for the parameters of interest is $f \in [20, 1024]$ Hz and $\tau \in [0.1, 100)$ ms, with the further constraint that f and τ have to yield physical masses and spins (i.e. $M_f > 0$ and $-1 < \chi_f < 1$).

IV. COMBINED RESULTS

A visual representation of the maximum posterior (MAP) waveforms resulting from the separated parameter estimation analyses is shown in Figure 4, with the template waveforms plotted on top of the detectors’ whitened strains. The probability distribution for the change in the area is obtained by combining the posterior distributions of the initial and final parameters from the selected inspiral and ringdown results.

The simulated binary black hole signal used in this paper is bound to agree with the area theorem by design. Using the fitting formulae in [47] we can estimate the expected area increase for the signal. Two non-spinning black holes with masses $M_1 = M_2 = 35M_\odot$ yield a final black hole with mass $M_f \simeq 66.6M_\odot$ and spin $\chi_f \simeq 0.69$, which translates into an expected area increase $A_f/A_i \simeq 1.56$.

The top panel in Figure 5 shows the measured area increase, with the expected value indicated by a red line. With current gravitational-wave detectors sensitivities (O1), the measured median value with 90% credible

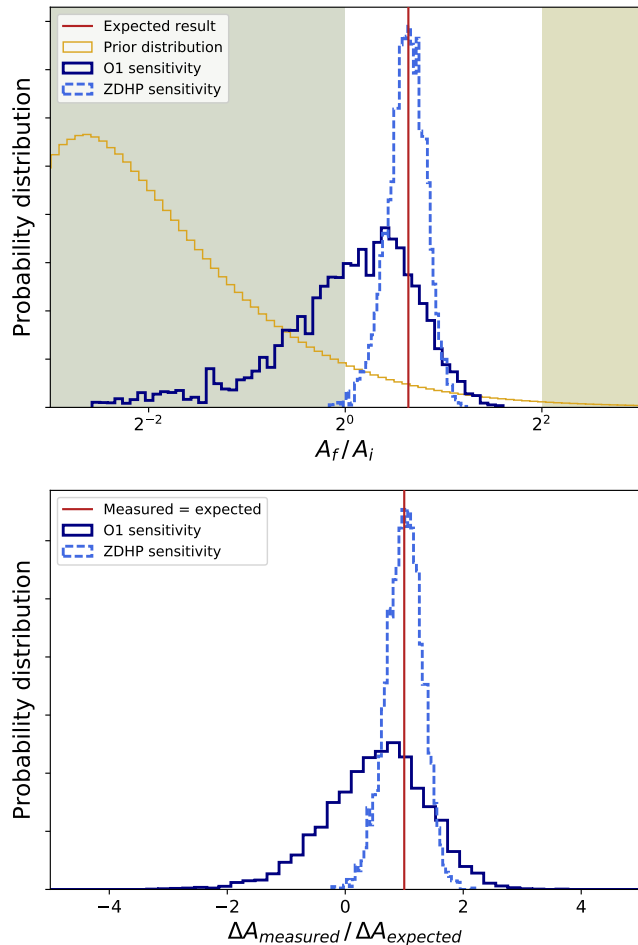


FIG. 5. (Top) Posterior distribution on the ratio of the final to initial areas, $A_f/(A_1 + A_2)$, for two different Advanced LIGO sensitivities, O1 and ZDHP. The shaded region $A_f/A_i < 1$ indicates violation of the area theorem, and $A_f/A_i > 4$ indicates violation of the conservation of energy. The vertical red line is the expected area increase. (Bottom) Distribution of the ratio $\Delta A_{\text{measured}}/\Delta A_{\text{expected}}$. The measured area change corresponds to the distribution shown in the top figure. The expected area change is given by the initial parameters obtained in the inspiral analysis and the corresponding expected final parameters from the fitting formulae in [47]. The vertical red line indicates agreement between the measured and the expected values, i.e. $\Delta A_{\text{measured}}/\Delta A_{\text{expected}} = 1$.

interval is $A_f/A_i = 1.31^{+0.84}_{-0.70}$. Furthermore, we obtain a $\sim 74.6\%$ probability that the simulated signal is consistent with the area theorem.

To ascertain how well we may test the area theorem in the future, we repeat the entire analysis on the same signal using the zero-detuned high-power (ZDHP) PSD from Ref. [43], which is the design sensitivity for Advanced LIGO. Figure 6 shows the JS divergence plots for the inspiral (top) and ringdown analyses (bottom). We find that the JS divergence of the inspiral (ringdown) posteriors settles to a constant value at $t_{\text{ref}} - 27.5$ ms

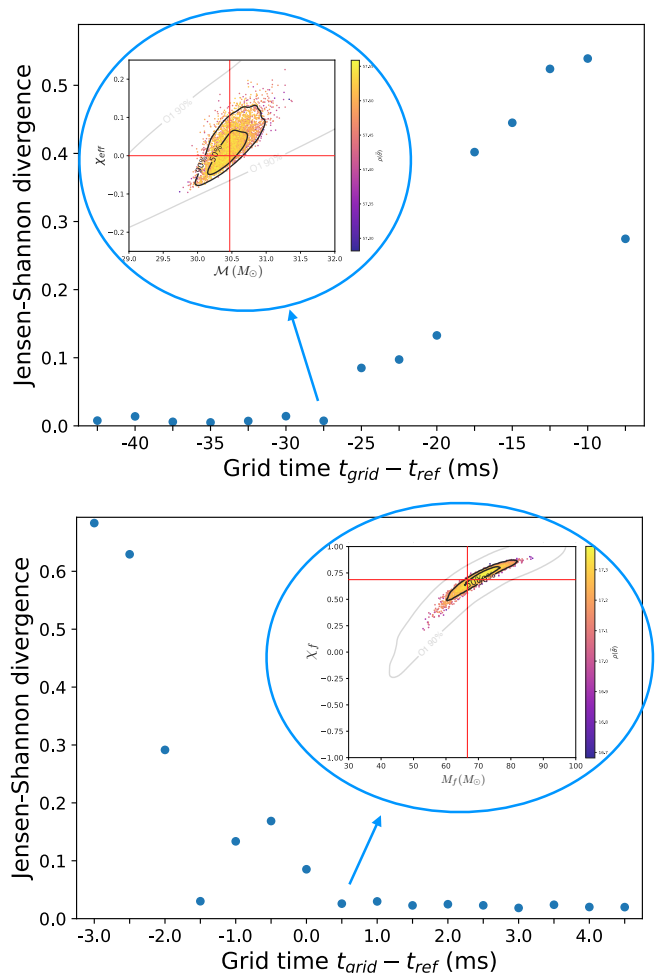


FIG. 6. Jensen-Shannon divergence between consecutive grid times of the inspiral (top) and ringdown (bottom) analyses using the ZDHP PSD. Insets show the resulting posterior distribution for the chosen transition times. The light grey posteriors correspond to the results obtained with O1 sensitivity. For the inspiral (ringdown) analysis we find that the JS divergence settles at $t_{\text{grid}} - t_{\text{ref}} = -27.5$ ms ($t_{\text{grid}} - t_{\text{ref}} = 0.5$ ms), consistent with the O1 PSD results shown in Fig. 2 (Fig. 3).

($t_{\text{ref}} + 0.5$ ms), which is the same as the O1 results. The selected ringdown grid time corresponds to $12.6 M_f$ after the peak amplitude of the signal. While here we have chosen the JS divergence as an estimate of the adequate ringdown time, there is no unique definition in the literature of the start of the ringdown [62–64].

Results with the ZDHP configuration are shown by the dashed posterior in Figure 5. In this case, the measured median value of the area increase with 90% credible interval is $A_f/A_i = 1.58^{+0.35}_{-0.33}$. With this sensitivity we obtain a $\sim 99.9\%$ probability that the simulated signal is consistent with the area theorem.

The median value of A_f/A_i underestimates the true value in the O1 results. This is primarily due to a systematic bias arising in the inspiral analysis. Both the mass ratio $q \equiv M_1/M_2$ ($M_1 \geq M_2$) and total mass are overes-

timated with this method; this leads to an overestimate of A_i by $\sim 10\%$, in turn leading to an underestimate of A_f/A_i . Further biasing the median is the fact that the simulated signal used here has $q = 1$. Since this is on the boundary of allowed parameter space, the median of the posterior distribution can only ever overestimate q , again leading to an underestimate of A_f/A_i . The chirp mass is well measured, therefore an overestimate in the mass ratio leads to an overestimate in the total mass as well. Finally, as seen in Figure 5, our prior on A_f/A_i strongly favours a violation of the area theorem. The prior follows from the uniform prior on the inspiral masses and spins and the uniform prior on the ringdown frequency and damping time. This also shifts the posterior distribution to smaller values of A_f/A_i , though the effect is small compared to the effect of the systematic bias.

Overall, the systematic bias in the area increase is less than the statistical error. Furthermore, as the bias is toward violations of the area theorem, it is a conservative error when evaluating the credible interval to which the signal is consistent with the area theorem.

Given the measured initial parameters from the inspiral analysis, one can obtain the expected area change for each point in the initial distribution using the fitting formulae in [47]. A direct comparison of the expected change with the measured change indicates the level of agreement of the final object with the fitting formulae, and therefore with general relativity. If the final object agrees with general relativity, the ratio between the measured and the expected values should be 1. The bottom panel in Figure 5 shows this ratio for the area change, $\Delta A = A_f - A_i$.

The independent measurements of the initial and final mass performed in this work also allow for estimating the energy radiated away by the system. The top panel in Figure 7 shows the posterior distribution in the energy radiated away, $\Delta E = E_i - E_f$, for both current and future Advanced LIGO sensitivities. The shaded region indicates the 29% bound derived from the area increase law. Similar as with the area change, one can compare the measured energy radiated, $\Delta E_{\text{measured}}$, with the result one would obtain making use of the fitting formulae in [47], $\Delta E_{\text{expected}}$. The bottom panel in Figure 7 shows the ratio between these two energies.

As can be seen by comparison of Figure 5 and Figure 7, the measurement of the area increase is more accurate than the measurement of the energy radiated. This can be understood from the lines of constant area shown in Figure 8. The area follows the ringdown posteriors better than the mass at positive spins, which are expected for two initially non-spinning black holes. Furthermore, we can expect the measurement of the area to be even sharper for highly aligned spinning black holes.

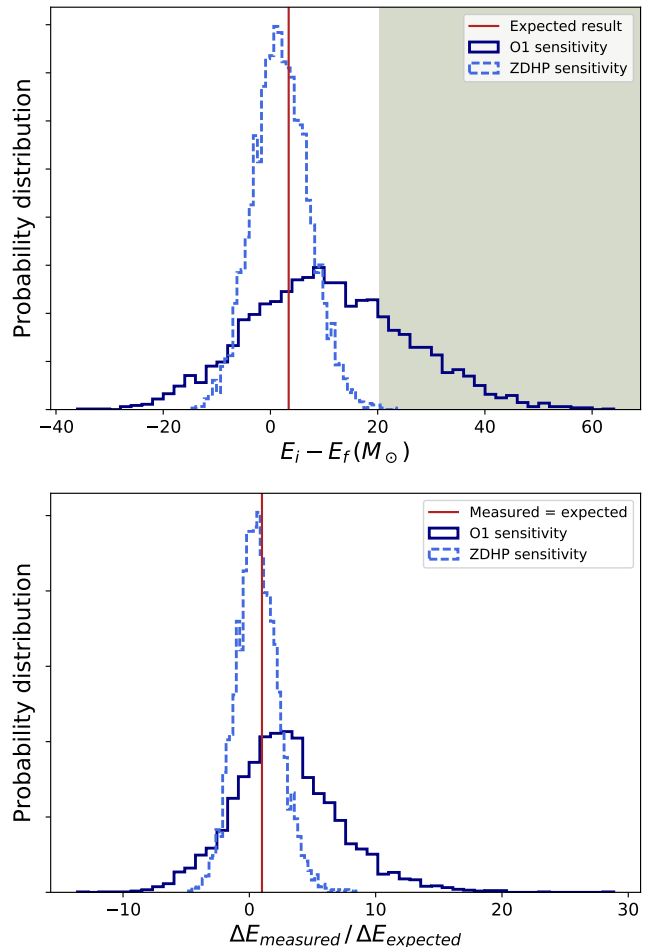


FIG. 7. (Top) Posterior distribution on the energy radiated during the coalescence. The red line indicates the expected value for the injected parameters, $E_i - E_f \simeq 3.4M_\odot$. The shaded region shows the theoretical limit of 29% in the energy emitted. (Bottom) Distribution of the ratio $\Delta E_{\text{measured}}/\Delta E_{\text{expected}}$. The expected radiated energy is given by the initial parameters obtained in the inspiral analysis and the corresponding expected final parameters from the fitting formulae in [47]. The vertical red line indicates agreement between the measured and the expected values, i.e. $\Delta E_{\text{measured}}/\Delta E_{\text{expected}} = 1$.

V. SIMULATING VIOLATIONS OF THE AREA THEOREM

In this Section we explore if we would be able to measure a violation of the area increase law with the method described above. We do not explore here how this violation could happen, but only if we would be able to measure a violation. For this purpose we compare our inspiral measurements with lower-mass ringdown signals. The spin of the final object is only dependent on the mass ratio and the spins of the initial objects. Changing the total mass of the binary will yield different final mass but the same final spin. Therefore, we find that

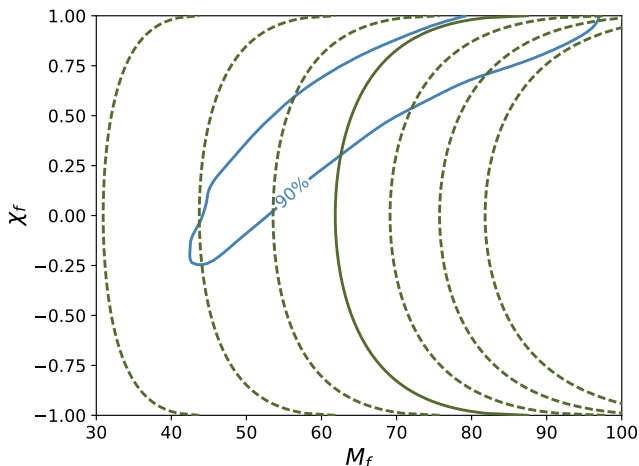


FIG. 8. Lines of constant area as function of the final mass and spin. The solid line shows the expected value, while dashed lines indicate areas $\pm 25\%$, 50% , 75% . For comparison, the 90% credible interval from the ringdown analysis with O1 sensitivity is shown.

for our system, a violation of the area theorem would require $M_f < 53.3M_\odot$. We use two ringdowns with masses $M_f \simeq 52.3M_\odot$ and $M_f \simeq 47.6M_\odot$, and perform the ringdown analysis only with the ZDHP sensitivity.

Figure 9 shows the result of combining these new ringdowns with the original inspiral results. The dashed posterior distribution with $\Delta M = M_f - M_t \simeq 3.4M_\odot$ is the result shown in the previous section. The continuous line with $\Delta M \simeq 17.7M_\odot$ is the system that yields a small violation of the area theorem. We find a $\sim 55.2\%$ probability that this system is in violation of the area theorem. The dotted line shows the system with even lower mass, for which we obtain $\sim 91.1\%$ probability that the system is in violation of the area theorem.

VI. CONCLUSIONS

We developed a method to test the area theorem on gravitational-wave signals from binary black hole coalescences. This method completely ignores information from the highly dynamical merger phase, thus ensuring that the initial and final parameters are measured independently from each other, and without assuming general relativity during the merger process.

With current gravitational-wave detectors sensitivities and zero noise, we obtained $\sim 74.6\%$ probability that a numerical waveform similar to GW150914 is consistent with the area theorem. This probability increases to $\sim 99.9\%$ with design sensitivity (ZDHP) for Advanced LIGO.

The next obvious step is to perform this analysis on a real gravitational-wave signal. From the binary black holes known to date there is only one with loud enough ringdown to perform this test: GW150914. We plan to

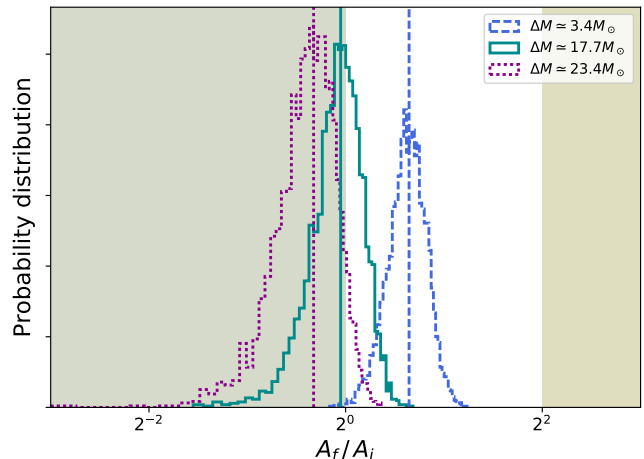


FIG. 9. Posterior distribution on the ratio of the final to initial areas, $A_f/(A_1 + A_2)$, with ZDHP sensitivity. The shaded region $A_f/A_i < 1$ indicates violation of the area theorem. The shaded region $A_f/A_i > 4$ indicates violation of the conservation of energy. Vertical lines indicate the expected value for each case. The dashed posterior distribution is the result shown in the previous section. The solid posterior distribution is a signal that slightly violates the area theorem, and the dotted posterior distribution is a signal that clearly violates the area theorem.

show results on this event in a future publication. One of the major issues is the choice of the start time for the ringdown. Our method of using the JS divergence will be a useful starting point for this analysis but might need to be refined for real data. In simulations with Gaussian noise, we have found that the qualitative behaviour of the JS divergence is the same as in Fig. 3, however the data has larger variations. This will be investigated in future work on real detector data.

The confidences obtained are mainly bound by the ringdown analysis, which yields wider posterior distributions than the inspiral analysis. Higher modes could start becoming important before the end of the second generation of gravitational-wave detectors. The addition of sub-dominant modes to the ringdown analysis will not only allow for tests of the Kerr nature of the final black holes, but could result in better constraints on the final mass and spin. Therefore, detectable higher modes could improve the confidence level on testing the area theorem.

As we have seen, the sky location is also an important limiting factor in our analysis. In this paper we have shown results on a two-detector network. However, the Virgo detector joined the second generation of gravitational-wave detectors in August of 2017, and showed an important contribution on sky localisation of gravitational-wave sources. Future events could therefore show different confidence levels as reported in this work if more than two detectors are being used.

The techniques we present may also be extended to make a joint measurement of the violation of the area

theorem for a population of binary black hole mergers. As an increasing number of mergers are detected, we expect that this may provide significant improvements to the overall uncertainties.

ACKNOWLEDGMENTS

We would like to thank Juan Calderón-Bustillo, Thomas Dent, Ben Farr, Will Farr, Domenico Giulini, David Keitel, Sebastian Khan, Andrew Lundgren, Frank Ohme and Reinhard Prix for interesting discussions. This research has made use of data, software and/or web tools obtained from the LIGO Open Science Centre (<https://losc.ligo.org>), a service of LIGO Laboratory and the LIGO Scientific Collaboration. LIGO is funded by the U.S. National Science Foundation.

-
- [1] S. W. Hawking, *Phys. Rev. Lett.* **26**, 1344 (1971).
 [2] S. W. Hawking, *Communications in Mathematical Physics* **25**, 152 (1972).
 [3] J. D. Bekenstein, *Lett. Nuovo Cim.* **4**, 737 (1972).
 [4] J. M. Bardeen, B. Carter, and S. W. Hawking, *Commun. Math. Phys.* **31**, 161 (1973).
 [5] J. D. Bekenstein, *Phys. Rev.* **D7**, 2333 (1973).
 [6] LIGO Scientific Collaboration and Virgo Collaboration, *Phys. Rev. Lett.* **116**, 061102 (2016), arXiv:1602.03837 [gr-qc].
 [7] LIGO Scientific Collaboration and Virgo Collaboration, *Phys. Rev. Lett.* **116**, 241103 (2016), arXiv:1606.04855 [gr-qc].
 [8] LIGO Scientific Collaboration and Virgo Collaboration, *Physical Review X* **6**, 041015 (2016).
 [9] LIGO Scientific Collaboration and Virgo Collaboration, *Phys. Rev. Lett.* **118**, 221101 (2017).
 [10] LIGO Scientific Collaboration and Virgo Collaboration, *Physical Review Letters* **119**, 141101 (2017).
 [11] S. A. Hughes and K. Menou, *Astrophys. J.* **623**, 689 (2005), arXiv:astro-ph/0410148 [astro-ph].
 [12] LIGO Scientific Collaboration and Virgo Collaboration (Virgo, LIGO Scientific), *Phys. Rev. Lett.* **119**, 161101 (2017), arXiv:1710.05832 [gr-qc].
 [13] LIGO Scientific Collaboration and Virgo Collaboration, *Phys. Rev. Lett.* **116**, 241102 (2016), arXiv:1602.03840 [gr-qc].
 [14] J. Healy, C. O. Lousto, and Y. Zlochower, *Phys. Rev.* **D90**, 104004 (2014), arXiv:1406.7295 [gr-qc].
 [15] F. Hofmann, E. Barausse, and L. Rezzolla, *The Astrophysical Journal Letters* **825**, L19 (2016).
 [16] X. Jiménez-Forteza, D. Keitel, S. Husa, M. Hannam, S. Khan, and M. Pürrer, *Phys. Rev.* **D95**, 064024 (2017), arXiv:1611.00332 [gr-qc].
 [17] A. Ghosh, A. Ghosh, N. K. Johnson-McDaniel, C. K. Mishra, P. Ajith, W. Del Pozzo, D. A. Nichols, Y. Chen, A. B. Nielsen, C. P. L. Berry, and L. London, *Phys. Rev.* **D94**, 021101 (2016), arXiv:1602.02453 [gr-qc].
 [18] A. Ghosh, N. K. Johnson-McDaniel, A. Ghosh, C. K. Mishra, P. Ajith, W. Del Pozzo, C. P. Berry, A. B. Nielsen, and L. London, *Classical and Quantum Gravity* **35**, 014002 (2017).
 [19] S. W. Hawking and G. F. R. Ellis, *The large scale structure of spacetime* (Cambridge University Press, 1976).
 [20] P. T. Chrusciel, E. Delay, G. J. Galloway, and R. Howard, *Annales Henri Poincaré* **2**, 109 (2001), arXiv:gr-qc/0001003 [gr-qc].
 [21] P. T. Chrusciel and G. J. Galloway, *Commun. Math. Phys.* **193**, 449 (1998), arXiv:gr-qc/9611032 [gr-qc].
 [22] J. Thornburg, *Living Rev. Rel.* **10**, 3 (2007), arXiv:gr-qc/0512169 [gr-qc].
 [23] A. Ashtekar and B. Krishnan, *Living Rev. Rel.* **7**, 10 (2004), arXiv:gr-qc/0407042.
 [24] I. Booth, *Can. J. Phys.* **83**, 1073 (2005), arXiv:gr-qc/0508107.
 [25] E.ourgoulhon and J. L. Jaramillo, *New Astron. Rev.* **51**, 791 (2008), arXiv:0803.2944 [astro-ph].
 [26] A. Ashtekar and B. Krishnan, *Phys. Rev.* **D68**, 104030 (2003), arXiv:gr-qc/0308033.
 [27] C. Barcelo and M. Visser, *Int. J. Mod. Phys.* **D11**, 1553 (2002), arXiv:gr-qc/0205066 [gr-qc].
 [28] I. Kamaretsos, M. Hannam, S. Husa, and B. S. Sathyaprakash, *Phys. Rev. D* **85**, 024018 (2012).
 [29] O. Dreyer, B. J. Kelly, B. Krishnan, L. S. Finn, D. Garrison, and R. Lopez-Aleman, *Class. Quant. Grav.* **21**, 787 (2004), arXiv:gr-qc/0309007 [gr-qc].
 [30] E. Berti, V. Cardoso, and A. O. Starinets, *Class. Quant. Grav.* **26**, 163001 (2009), arXiv:0905.2975 [gr-qc].
 [31] S. Gossan, J. Veitch, and B. S. Sathyaprakash, *Phys. Rev. D* **85**, 124056 (2012).
 [32] N. Yunes, K. Yagi, and F. Pretorius, *Phys. Rev.* **D94**, 084002 (2016), arXiv:1603.08955 [gr-qc].
 [33] V. Baibhav, E. Berti, V. Cardoso, and G. Khanna, *Physical Review D* **97**, 044048 (2018).
 [34] L. Smarr, A. Cadez, B. S. DeWitt, and K. Eppley, *Phys. Rev.* **D14**, 2443 (1976).
 [35] J. Healy, I. Ruchlin, C. O. Lousto, and Y. Zlochower, *Phys. Rev.* **D94**, 104020 (2016), arXiv:1506.06153 [gr-qc].
 [36] T. A. Apostolatos, C. Cutler, G. J. Sussman, and K. S. Thorne, *Phys. Rev.* **D49**, 6274 (1994).
 [37] P. Jaranowski, A. Krolak, and B. F. Schutz, *Phys. Rev.* **D58**, 063001 (1998), arXiv:gr-qc/9804014 [gr-qc].
 [38] I. Mandel, C. P. L. Berry, F. Ohme, S. Fairhurst, and W. M. Farr, *Class. Quant. Grav.* **31**, 155005 (2014), arXiv:1404.2382 [gr-qc].
 [39] <http://www.black-holes.org/waveforms>.
 [40] A. H. Mroue, M. Scheel, B. Szilagyi, H. Pfeiffer, M. Boyle, D. Hemberger, L. Kidder, G. Lovelace, S. Ossokine, N. Taylor, A. Zenginoglu, L. Buchman, T. Chu, E. Foley, M. Giesler, R. Owen, and S. Teukolsky, *Phys. Rev. Lett.* **111**, 241104 (2013), arXiv:1304.6077 [gr-qc].
 [41] L. London, D. Shoemaker, and J. Healy, *Phys. Rev. D* **90**, 124032 (2014).

- [42] M. Vallisneri, J. Kanner, R. Williams, A. Weinstein, and B. Stephens, *Journal of Physics: Conference Series* **610**, 012021 (2015).
- [43] D. Shoemaker, *Advanced LIGO anticipated sensitivity curves*, Tech. Rep. (LIGO T0900288-v3, 2009).
- [44] C. M. Biwer, C. D. Capano, S. De, M. Cabero, D. A. Brown, A. H. Nitz, and V. Raymond, (2018), arXiv:1807.10312 [astro-ph].
- [45] J. Veitch, V. Raymond, B. Farr, W. Farr, P. Graff, S. Vitale, B. Aylott, K. Blackburn, N. Christensen, M. Coughlin, W. DelPozzo, F. Feroz, J. Gair, C. Haster, V. Kalogera, T. Littenberg, I. Mandel, R. OShaughnessy, M. Pitkin, C. Rodriguez, C. Rover, T. Sidery, R. Smith, M. VanDerSluys, A. Vecchio, W. Vousden, and L. Wade, *Phys. Rev.* **D91**, 042003 (2015), arXiv:1409.7215 [gr-qc].
- [46] B. Farr and W. M. Farr, In prep.
- [47] S. Husa, S. Khan, M. Hannam, M. Pürrer, F. Ohme, X. Jiménez-Forteza, and A. Bohé, *Phys. Rev. D* **93**, 044006 (2016).
- [48] S. Khan, S. Husa, M. Hannam, F. Ohme, M. Pürrer, X. Jiménez-Forteza, and A. Bohé, *Physical Review D* **93**, 044007 (2016), arXiv:1508.07253 [gr-qc].
- [49] S. Klimentenko, G. Vedovato, M. Drago, F. Salemi, V. Tiwari, G. Prodi, C. Lazzaro, K. Ackley, S. Tiwari, C. DaSilva, and G. Mitselmakher, *Phys. Rev.* **D93**, 042004 (2016), arXiv:1511.05999 [gr-qc].
- [50] A. Buonanno, B. R. Iyer, E. Ochsner, Y. Pan, and B. S. Sathyaprakash, *Phys. Rev.* **D80**, 084043 (2009), arXiv:0907.0700 [gr-qc].
- [51] M. Cabero, A. B. Nielsen, A. P. Lundgren, and C. D. Capano, *Phys. Rev.* **D95**, 064016 (2017), arXiv:1602.03134 [gr-qc].
- [52] F. F. Kuo and J. F. Kaiser, *System analysis by digital computer* (Wiley, 1966).
- [53] J. A. Thomas and T. M. Cover, *Elements of Information Theory* (Wiley-Interscience, 1991).
- [54] D. M. Endres and J. E. Schindelin, *IEEE Transactions on Information Theory* **49**, 1858 (2003).
- [55] E. Berti, V. Cardoso, and A. O. Starinets, *Classical and Quantum Gravity* **26**, 163001 (2009).
- [56] S. Chandrasekhar, *The mathematical theory of black holes* (1985).
- [57] E. W. Leaver, *Proc. Roy. Soc. Lond.* **A402**, 285 (1985).
- [58] K. D. Kokkotas and B. G. Schmidt, *Living Rev. Rel.* **2**, 2 (1999), arXiv:gr-qc/9909058 [gr-qc].
- [59] E. Berti, V. Cardoso, and M. Casals, *Phys. Rev. D* **73**, 024013 (2006).
- [60] E. Berti, J. Cardoso, V. Cardoso, and M. Cavaglià, *Phys. Rev. D* **76**, 104044 (2007).
- [61] E. Berti, V. Cardoso, and C. M. Will, *Phys. Rev. D* **73**, 064030 (2006).
- [62] E. Thrane, P. D. Lasky, and Y. Levin, *Phys. Rev.* **D96**, 102004 (2017), arXiv:1706.05152 [gr-qc].
- [63] S. Bhagwat, M. Okounkova, S. W. Ballmer, D. A. Brown, M. Giesler, M. A. Scheel, and S. A. Teukolsky, *Physical Review D* **97**, 104065 (2018).
- [64] V. Baibhav, E. Berti, V. Cardoso, and G. Khanna, *Phys. Rev. D* **97**, 044048 (2018).